

Generated using the official AMS L<sup>A</sup>T<sub>E</sub>X template v6.1 two-column layout. This work has been submitted for publication. Copyright in this work may be transferred without further notice, and this version may no longer be accessible.

## The Role of Deep Mesoscale Eddies in Ensemble Forecast Performance

JUSTIN P. COOKE,<sup>a</sup> KATHLEEN A. DONOHUE,<sup>a</sup> CLARK D. ROWLEY,<sup>b</sup> PRASAD G. THOPPIL,<sup>b</sup> D. RANDOLPH WATTS,<sup>a</sup>

<sup>a</sup> Graduate School of Oceanography, University of Rhode Island, Narragansett, Rhode Island

<sup>b</sup> Ocean Sciences Division, Naval Research Laboratory, Stennis Space Center

**ABSTRACT.** Present forecasting efforts rely on assimilation of observational data captured in the upper ocean (< 1000 m depth). These observations constrain the upper ocean and minimally influence the deep ocean. Nevertheless, development of the full water column circulation critically depends upon the dynamical interactions between upper and deep fields. Forecasts demonstrate that the initialization of the deep field is influential for the development and evolution of the surface in the forecast. Deep initial conditions that better agree with observations have lower upper ocean uncertainty as the forecast progresses. Here, best and worst ensemble members in two 92-day forecasts are identified and contrasted in order to determine how the deep ocean differs between these groups. The forecasts cover the duration of the Loop Current Eddy Thor separation event, which coincides with available deep observations in the Gulf. Model member performance is assessed by comparing surface variables against verifying analysis and satellite altimeter data during the forecast time-period. Deep cyclonic and anticyclonic features are reviewed, and compared against deep observations, indicating subtle differences in locations of deep eddies at relevant times. These results highlight both the importance of deep circulation in the dynamics of the Loop Current system and more broadly motivate efforts to assimilate deep observations to better constrain the deep initial fields and improve surface predictions.

### 1. Introduction

The Loop Current (LC) system (GoM; Fig. 1) is the primary forcing mechanism for mesoscale oceanographic variability in the Gulf of Mexico (Oey 2008). The LC brings warm, salty waters from the Caribbean Sea *via* the Yucatán Channel, exiting through the Straits of Florida. Flow may enter and exit in a retracted port-to-port mode, or it may extend into the Gulf as a northward loop as far as 28°N and 93°W. As the LC extends, it eventually pinches off a closed warm core, anticyclonic eddy with horizontal scales of 200-400 kilometers, known as a Loop Current Eddy (LCE). The LCE may reattach or shed, advecting west, with an observed shedding frequency ranging from weeks to months (Sturges and Leben 2000; Leben 2005). Before its eventual separation, the LCE may undergo multiple instances of detachment and reattachment (Leben 2005; Tsei et al. 2025). LCEs carry significant energy and strong currents, affecting transport of heat and momentum, with implications for hurricanes (Le Hénaff et al. 2021), fisheries (Cornic and Rooker 2018; Gilmartin et al. 2020) and offshore energy industries such as oil and gas (National Academies of Sciences and Medicine 2018). By good fortune, during the 2010 *Deepwater Horizon* oil spill, peripheral eddies generated by the LC were observed to have entrapped some of the oil, preventing it from continuing through the Straits of Florida (Hiron et al. 2020). Improving our understanding of the LC system, and the mechanisms contributing to LCE separation, is critical for ensuring both the safety of the communities around the Gulf, and for responsible operation by industries in the region.

Numerous studies – ranging from numerical (Hurlburt and Thompson 1982; Oey 2008; Chang and Oey 2011; Le Hénaff et al. 2012; Dukhovskoy et al. 2015), observational (Candela et al. 2002; Donohue et al. 2016; Sheinbaum et al. 2016), and theoretical (Pichevin and Nof 1997; Nof 2005), among many others – have investigated the physics of LCE separation. Availability of altimeter derived surface measurements, along with an abundance of instruments operating in the upper 1000 meters, has resulted in a focus on upper oceanic processes and their impact (Schmitz Jr 2005; Sheinbaum et al. 2016; Androulidakis et al. 2021; Laxenaire et al. 2023). A prominent theme is that Loop Current Frontal Eddies (LCFEs) contribute significantly to the eddy shedding process (Schmitz Jr 2005; Le Hénaff et al. 2012). These eddies contain horizontal scales  $\sim O(10 - 100)$  kilometers, reaching depths of 1000 meters, and form at the periphery of the LC, near the Campeche Bank (see Fig. 1; Oey 2008; Sheinbaum et al. 2016). However, prior work has also demonstrated the existence of deep, mesoscale eddies in the Gulf (Oey 2008; Hamilton 2009; Donohue et al. 2016; Hamilton et al. 2016; Pérez-Brunius et al. 2018; Johnson Exley et al. 2022; Safaie et al. 2025). These eddies exist below 1000 meters and interact with the upper baroclinic jet through upper-deep vortex stretching, related to baroclinic instability (Hamilton 2009; Le Hénaff et al. 2012; Donohue et al. 2016), but their role in LCE shedding is still not fully understood (Hamilton et al. 2019). Increased interest in the deep currents of the Eastern Gulf led to a recent investigation from Morey et al. (2020), who highlighted differences between deep observations and models: notably that contemporary models vastly underestimate deep eddy kinetic energy levels generated during the LCE separation process.

---

Corresponding author: Justin P. Cooke, justin.cooke@uri.edu

A study from Rosburg et al. (2016) demonstrated that models tend to underestimate the eddy kinetic energy (EKE) in the deep by a factor of three. Nevertheless, despite these discrepancies in modeling deep energy, forecasts appear to reasonably represent the LC system (Wei et al. 2016; Thoppil et al. 2025).

Numerical models are used to forecast the ocean with Data Assimilation (DA), where observational data is used to initialize the model to predict future states (Stammer et al. 2016). Forecasts can be run in single deterministic configurations, or as an Ensemble Forecast (EF) with multiple members that represent the best guess for a predictive state of a dynamical system (Wei et al. 2008). Recent work from Thoppil et al. (2021) demonstrated improved forecast skill – by nearly a factor of three – of ocean mesoscales for a lower resolution EF, compared against a higher resolution deterministic forecast. Forecast members may differ within the range of their error covariance – the matrix composed of the variance of individual errors, and how they are related to other errors in the system – which accounts for observational uncertainty in the initial conditions (Martin et al. 2015). Others use entirely different modeling schemes altogether, known as multimodel super-ensembles (Krishnamurti et al. 1999). EFs tend to only assimilate surface data from satellites, such as sea surface height (SSH) and sea surface temperature (SST), or temperature and salinity profiles from *in situ* observational platforms – ARGO floats, CTDs, and gliders (Rosburg et al. 2016; Wei et al. 2016). A recent study from Dukhovskoy et al. (2023) substantiated improved model performance in predicting deep flow in the Gulf when assimilating Current and Pressure recording Inverted Echo Sounder (CPIES) data, which provide temperature and salinity profiles for the full depth of the water column.

Here, we demonstrate the impact of the unconstrained deep field on ensemble forecast performance during the LCE Thor Separation event, which spanned October 28th, 2019 through April 6th, 2020. This event was challenging from a forecast perspective, as LCE Thor detached, and eight weeks later reattached and then separated. An analysis of eleven weekly ensemble forecasts between October 28th, 2019 through January 6th, 2020 reveal that the initial conditions that agree better with deep observations produce improved upper forecasts 5 and 6 weeks later. Then proceeding from this finding, we examine the coupled upper-deep processes developing during two ensemble forecast periods, one beginning October 28th, 2019 and the other on January 6th, 2020, described in greater detail in Thoppil et al. (2025), which were effective in predicting the complex separation process.

We implement a strategy to identify the best and worst performing ensemble members, based on SSH, using two different benchmarks to compare method robustness. The deep fields for the two groups are contrasted to identify the differences leading to their predictions. Moreover, mapped

observations of the deep fields from CPIES are available during this time-period, allowing for direct comparison. Our work highlights how deep observations could be effectively used by regional ensemble forecasts in strong current regimes to improve forecasts.

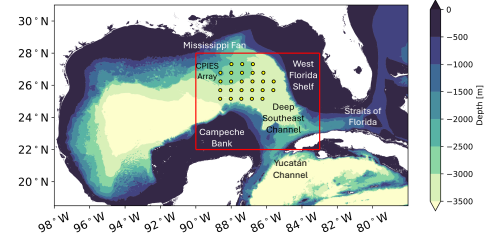


FIG. 1. The Gulf of Mexico with the region of interest (red box), which ranges from 22°N to 28°N, 90°W to 83°W. The Understanding Gulf Ocean Systems CPIES array (black, yellow-filled circles), and names of key features are included. Bathymetry is contoured every 500 meters.

## 2. Methodology

### a. Ensemble Forecast Model

The Naval Research Laboratory runs a 32-member Ensemble Forecast system in the Gulf of Mexico. This forecast system combines the Navy Coastal Ocean Model (NCOM; Martin et al. 2009) with the Navy Coupled Ocean Data Assimilation system (NCODA; Cummings 2005), as well as the Coupled Ocean-Atmosphere Mesoscale Prediction System (COAMPS; Hodur 1997). The domain includes the entire Gulf of Mexico (Fig. 1), and has 3 km horizontal resolution and 49 hybrid levels in the vertical. The vertical levels are split into 33 sigma (terrain/surface following) levels and below that 16 z-, or pressure, levels; the finest resolution is near the surface, becoming coarser with depth. Vertical mixing is parametrized with the Mellor-Yamada level 2 turbulence closure scheme (Mellor and Yamada 1982). Lateral boundary conditions are handled as tides, and monthly mean transports are used for riverine input. To allow for assimilation of all available observations, the model is initialized from an NCODA analysis product.

The NCODA system deploys a 3-D Variational (3DVar) assimilation scheme, allowing for near real-time inclusion of observations, such as satellite altimeter products (SSH and SST), as well as profiles from gliders, floats, and ships. Satellite altimeter observations are incorporated into the model via the Modular Ocean Data Assimilation System (MODAS); MODAS synthesizes temperature and salinity profiles from SSH and SST, projecting them down through the water column to constrain the ocean interior (Fox et al. 2002). Velocity information is not assimilated into the forecast system.

In order to account for a variety of physically realizable and dynamically relevant ocean states, model initial conditions are perturbed. The perturbations are formulated from the 24-hour forecast error variances of a control run, which represent model and observation uncertainties in a single deterministic forecast, using the Ensemble Transform method (Bishop and Toth 1999; Wei et al. 2006). Additionally, estimates of the model temporal variability and climate variability are added to ensure a similar spread of the ensemble model perturbations to the error variance of the best guess control run.

Ensemble forecasts from two starting dates are analyzed, chosen to span the entirety of the LCE Thor separation event. The focus region of the study is the Eastern Gulf, where the LCE separation occurs, bounded by 22°N to 28°N, 83°W to 90°W (red box in Fig. 1). The first 92-day ensemble forecast begins on October 28th, 2019, and ends January 27th, 2020, and is referred to as EF20191028. This forecast successfully predicted the timing of the initial detachment of the LCE, occurring around January 10th, coinciding with the presence of a cyclonic eddy in the region of the Deep Southeast Channel (DSC; Fig. 1). The second forecast begins on January 6th, 2020, and ends April 6th, 2020, and is referred to as EF20200106. This time-period covers the observed reattachment of the LCE near March 16th, and final separation around March 30th, associated with a deep cyclone moving south and westward off the Mississippi Fan (Fig. 1).

### b. Observations

Two datasets are used to assess model member performance: an array of Current Pressure Inverted Echo Sounders (CPIES) and satellite sea surface height derived from E.U. Copernicus Marine Service Information (CMEMS) (1993). Twenty-four CPIES (black, yellow-filled circles in Fig. 1) were deployed for almost two years, June 2019 through May 2021 and span the LCE Thor separation event. The array extended from 25°N to 27.5°N, 86°W to 89°W, with approximately 60 km spacing between instruments (Johnson Exley et al. 2022). Here we focus on the near-bottom pressure and current CPIES records. Details regarding CPIES processing can be found in Johnson Exley et al. 2022. Pressure and currents are low-pass filtered with a 72-hour cutoff, and subsampled in 12-hour increments. Bottom pressure maps are generated using a multivariate optimal interpolation approach, which constrains pressure and velocity to be geostrophic, and with the deep velocity observations, sharpen the gradients (Watts et al. 2001).

For comparisons to estimate the accuracy of the forecast SSH fields, we use global CMEMS satellite data from October 28th, 2019 to April 6th, 2020 from 22°N to 28°N, 80°W to 90°W. The data consists of Absolute Dynamic Topography (ADT) which is daily averaged and gridded with

0.125° × 0.125° horizontal resolution. For consistency in the analysis, we remove daily spatial means from the SSH fields, such that the 17-cm contour line, representative of the LC and LCE fronts (Leben 2005), may be tracked and used for comparison against the model.

### c. Identification of Deep Mesoscale Eddies

To represent deep circulation and mesoscale eddies in the model data, we calculate the deep reference pressure by expressing the total sea surface height ( $\eta_{total}$  [m]) as the sum of the reference ( $\eta_{ref}$  [m]) and steric ( $\eta_{steric}$  [m]) components. Use of  $\eta_{ref}$  is advantageous in its simplicity – eddies are identified using this scalar stream function, as opposed to a more highly differentiated scalar parameter like relative vorticity. This stream function enables a straightforward visualization of the deep fields, allowing for the determination of deep, mesoscale features.

$$\eta_{total} = \eta_{ref} + \eta_{steric}. \quad (1)$$

The reference height may be converted to a reference pressure with units of Pascals (Pa),  $\eta_{ref} \equiv P_{ref}/(\rho_b g)$ , where  $\rho_b$  is bottom density and  $g$  is gravity. The steric component is found by the geopotential height anomaly ( $\phi$ ), divided by the acceleration due to gravity. We can determine  $\phi$  by integrating from the surface ( $P_1 = 0$  dbar) to a constant reference pressure,  $P_2 \approx 2023$  dbar (equivalently 2000 m depth),

$$\phi = \int_{P_1}^{P_2} \delta dP, \quad (2)$$

where  $\delta$  is the specific volume anomaly,

$$\delta = \frac{1}{\rho(S, T, P)} - \frac{1}{\rho(S_0, T_0, P)}. \quad (3)$$

Here,  $\rho$  is the density,  $S$  is salinity, and  $T$  is temperature, with reference values  $S_0 = 35$  psu and  $T_0 = 0^\circ\text{C}$ .

## 3. The Deep Field and SSH Prediction

Deep mesoscale eddies can interact with the upper layer through vortex stretching. Upper and deep layer interaction may occur in two ways. First, deep eddies are depth-independent, maintaining a uniform vertical structure throughout the water column; their associated reference velocities can add normal components crossing the upper layer baroclinic currents (Donohue et al. 2016). Second, this interaction produces vertical stretching by the deep layer exerted on the upper. In this interaction the deep layer influences the upper layer, when its deep reference current has a component perpendicular to the slope of the upper layer isopycnals. Thus its depth-independent, nearly isopycnal component produces upper layer vertical stretching. Conversely, the upper layer exerts influence on the deep when upper baroclinic fronts shift laterally

and the sloped isopycnals produce vertical stretching of the weakly stratified lower layer. These two mechanisms occur together in baroclinic instability for instances where there is a favorable vertical offset of perturbations between upper and deep eddy variability.

The impact of uncertainty in the deep field to forecast success is highlighted in (Fig. 2) which shows the relationship between the initial, Week 0, root-mean-square-error (RMSE)  $\eta_{ref}$  against weekly SSH RMSE. Here, we use the verifying analysis as a benchmark because it constitutes the initial ocean state for each subsequent weekly long-range ensemble forecast and assimilates observations; therefore, it represents the most realistic ocean state. For  $\eta_{ref}$  RMSE, we used Week 0 forecast ensemble mean and the observed CPIES  $\eta_{ref}$  in the region 22°N to 28°N, 90°W to 83°W (see Fig. 1). Eleven weekly 92-day, 32-member ensemble forecasts during the LCE Thor time-period, from October 28th, 2019 through January 6th, 2020 are used in the analysis. Forecasts are referred to in the following manner: EFYYYYMMDD, where the date is the start of the forecast, *i.e.*, October 28th, 2019 is EF20191028. Three notable results emerge:

- Figure 2a indicates weak dependence of the initial uncertainty of the deep  $\eta_{ref}$  field on the stage of the LC cycle, as the earlier forecasts begin with a more retracted LC, with other forecasts beginning with an LC extended further into the Gulf, or a detached LCE.
- Better initial conditions in the deep  $\eta_{ref}$  field yield lower uncertainty in the upper SSH field as the forecast progresses, as indicated by the linear trend found as the forecasts progress (Fig. 2).
- By the sixth forecast week, a strong dependence is evident of the outcome upon the initialization. The members that have highest uncertainty in SSH, are approximately six weeks out from the initial detachment of LCE Thor, exemplified by two consecutive forecasts, EF20191125 (left triangle) and EF20191202 (square), which show highest uncertainty at Week 6 (Fig. 2f).

To highlight the difference between a “better” and “poor” initial deep field, we plot the ensemble mean  $\eta_{ref}$  field at 2000 meters for EF20191028 (top row in Fig. 3) and EF20191125 (bottom row in Fig. 3), these correspond to the two filled symbols (circle and left triangle) in Fig. 2, respectively. Model  $\eta_{ref}$  field at Week 0 and Week 6 is contrasted with the CPIES observations, and the mean 17-cm contour of the forecast (cyan line) against the verifying analysis 17-cm contour (black line). Between the two forecasts, the initial field for EF20191028 contains more similar features as seen in the observations, including the more northern cyclone coupled with an anticyclonic feature to its south, whereas the initial field for EF20191125

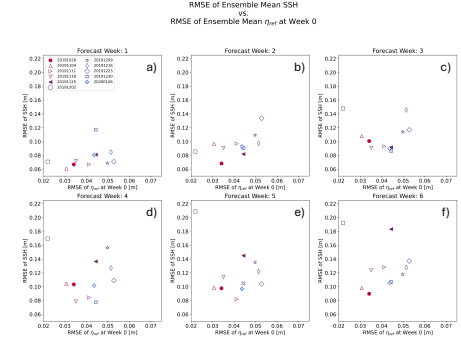


FIG. 2. Scatter plot of RMSE of  $\eta_{ref}$  from different forecasts at Week 0 compared against the observations from the CPIES array, plot against RMSE of SSH for each forecast's respective a) Week 1, b) Week 2, c) Week 3, d) Week 4, e) Week 5, and f) Week 6. Deep mean fields for  $\eta_{ref}$  are shown in Fig. 3 for the filled symbols.

shows a strong anticyclone-cyclone dipole at 88°W that is not present in the observations, and a stronger anticyclonic feature that the CPIES observations show is much weaker near 86°W. As the forecast evolves, these initial conditions result in a better predicted deep field at Week 6 for EF20191028, with both the model and the observations displaying an anticyclone off the Mississippi Fan. This is also reflected in the good agreement between the predicted 17-cm contour (cyan line) of the forecast, and the 17-cm contour of the verifying analysis on that date (black line). In contrast, the deep field of EF20191125 shares no similarities with the CPIES observations, and shows a larger, detached LCE with a still extended LC. These findings imply a connection between deep skill and upper performance.

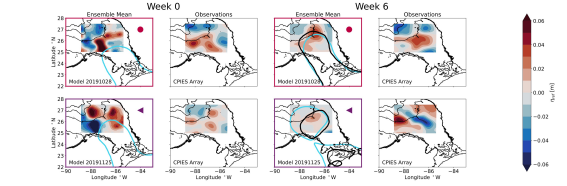


FIG. 3. Deep ensemble mean  $\eta_{ref}$  fields for EF20191028 (top row) and EF20191125 (bottom row), exemplifying a “better” initial condition and a “poor” initial condition, respectively. Model fields are contrasted against the CPIES observations at Week 0 (left columns) and Week 6 (right columns). The purple lines represent the 17-cm contour for the forecast, and the black lines at Week 6 represent the 17-cm contour for the verifying analysis.

#### 4. Assessment of Ensemble Forecast Member Performance

Two forecasts, EF20191028 and EF20200106, provide case studies to illustrate the relationship between upper

and deep circulation. The first forecast, EF20191028, predicted the initial detachment of LCE Thor, and the second forecast, EF20200106, captured the reattachment and final separation of LCE Thor. As a first step, best and worst performing members are isolated. The selection process is presented in the next section.

#### a. Best and Worst Member Selection

Figure 4 outlines the procedure for selecting the best and worst members. Across all members, we calculate the RMSE of a parameter of interest between the forecast and our chosen benchmark, at weekly intervals. We sort members from lowest to highest RMSE, and use the 80<sup>th</sup> and 20<sup>th</sup> percentiles as cutoffs; the members within lowest and highest percentiles are recorded by week. The number of appearances for each member in each percentile is recorded, sorting from most to least. For each group, using the upper 80<sup>th</sup> percentile, we determine the best and worst members over the whole forecast time-period. This selection process is generalizable to any desired variable.

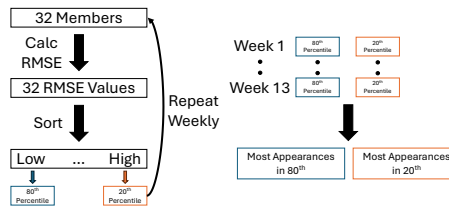


FIG. 4. Schematic flow chart for member selection.

This study focuses on comparing SSH, due to forecasts only assimilating data from the upper ocean. We use two benchmarks: i) the verifying analysis; and ii) a gridded satellite product. Note, we alternatively tested using surface velocity, but because we found a linear relationship between SSH RMSE and surface velocity RMSE, we dismissed the latter parameter (see Appendix A). Additionally, we investigated using a method with information in the upper 500 meters of the water column, composed of SSH, temperature ( $T$ ), salinity ( $S$ ), zonal velocity ( $U$ ), and meridional velocity ( $V$ ) from the verifying analysis. A weighted RMSE value was found at each depth, and used for ranking. This method selected a majority of the same members – for both the best and worst groups – for each forecast, so we choose to use the simpler method which requires only SSH (see Appendix B).

#### b. Selecting for EF20191028

We select the best and worst members using weekly RMSE of SSH compared against i) the verifying analysis and ii) gridded SSH derived from satellite altimeter product of E.U. Copernicus Marine Service Information (CMEMS) (1993). A majority of the selected members

(four of six) are shared between the benchmarks for both the best members and worst members, highlighting the robustness of the selection method. A possible reason for the minor difference in member selection may result from the verifying analysis containing observational information in addition to satellite-derived data. Moreover, the horizontal resolution in the model grid is approximately a factor of four times finer than the satellite resolution. Despite this, the benchmarks agree well on which members do, and do not, capture SSH and the position of the LC.

We plot the weekly RMSE of SSH for the two benchmarks in Fig. 5. For both, the spread of uncertainty is low over the first four weeks (11/04 to 11/25) with little distinction between the best and worst members. After the fifth week (12/02), the two groups separate, with the best members maintaining consistently lower RMSE values over the next five weeks (through 01/06). At the point of detachment for LCE Thor (01/13) and in the subsequent weeks, the best members maintain lower RMSE values of SSH compared against the mean. Remarkably, half of the members in the worst group improve, especially by the final week of the forecast (01/27), for both benchmarks. For the ensemble mean, current forecast skill for SSH only extends for 5–6 weeks (Thoppil et al. 2025); hence, performance for the following weeks have higher uncertainty, especially in individual members. Despite this, we have confidence that the best (worst) members determined in the selection process are consistently the best (worst) over the majority of the forecast.

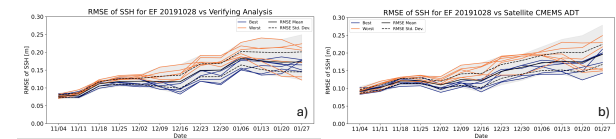


FIG. 5. Weekly RMSE of SSH for EF20191028 compared against a) the verifying analysis and b) the CMEMS satellite product. Only the best (blue, solid lines) and worst (orange, solid lines) members are shown. The range (gray, shaded-region) is bounded by the weekly maximum and minimum values of RMSE. The mean of RMSE values (black, solid line) and one standard deviation above and below this mean (black, dashed lines) are provided.

#### c. Selecting for EF20200106

We repeat the selection process for EF20200106, which includes the time-period of the reattachment and final separation of LCE Thor. As with EF20191028, the majority (four of six) of the best and the worst members are shared by the two benchmarks. This is especially encouraging due to the complex nature of the reattachment and separation occurring in this time-period. Figure 6 displays the weekly values of SSH RMSE. It is notable that the RMSE using the verifying analysis maintains better agreement – lower maximum and minimum RMSE values – over the forecast

time-period, when compared to the CMEMS satellite product; however, the spread of the uncertainty is much larger, especially by the final week of the forecast. In contrast, the RMSE using the CMEMS satellite product has lower spread in the uncertainty and higher RMSE values, with a marked increase in slope of the RMSE occurring after the fifth week (02/10). This behavior was not observed in the October 2019 forecast (Fig. 5), as both benchmarks resulted in similar spread in uncertainty and maintained similar values over that time-period. We attribute this to the different stage in LCE separation process observed in each forecast.

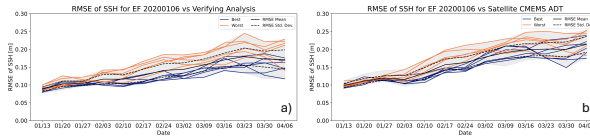


FIG. 6. Weekly RMSE of SSH for EF20200106 compared against a) the verifying analysis and b) the CMEMS satellite product. Colors and line-types are the same as Fig. 5

Much like the prior forecast, for both, the range of uncertainty is minimal over the first four weeks (01/13 through 02/03), and there is little differentiation between best and worst members. For the verifying analysis at Week 5 (02/10), the uncertainty of the two groups becomes dissimilar, and between this week and shortly before the reattachment at Week 9 (03/09), the best (worst) members selected by the verifying analysis (Fig. 6a) display consistently lower (higher) RMSE values than the mean of the RMSE (black, solid line). Through the reattachment at Week 10 (03/16) to the final separation at Week 12 (03/30), a majority of the best members maintain their lower values of RMSE, compared against the mean of all RMSE values. We note some overlap between individual members of the best and worst groups is observed in Fig. 6a, but overall the worst members tend to display higher values of RSME during the forecast time-period. In contrast, the difference between the best and worst members is not as definitive with the CMEMS satellite product (Fig. 6b). The two groups maintain distinction between Week 5 (02/10) and shortly before the reattachment (03/02); however, an increase in RMSE occurs for some of the best performing members with the opposite occurring for some of the worst performing members at the reattachment (03/09). Despite this, by the time of the final separation of LCE Thor at Week 12 (03/30), the majority of the best members maintain lower uncertainty than the mean RMSE. Conversely, some of the worst members maintain RMSE values lower than the mean at this week. These results demonstrate the challenging nature in forecasting the reattachment and final separation of LCE Thor, and possibly indicates why the ensemble mean of the forecast performed so well during this time-period. Although the uncertainty was larger when

comparing the forecast against a satellite derived SSH, the spread of this uncertainty was lower, and we found that even those members that were initially doing poorly eventually improved.

## 5. Structure of the Deep Eddy Field

### a. EF20191028: Importance of Eddy Magnitude and Position

To better understand the differences between the best and worst members, we review the deep field with a focus on the structure, location and propagation of mesoscale eddies. Figure 7 shows the mean upper and deep fields for the best and worst members. Weekly RMSE plots (Fig. 5) indicated little difference in Weeks 1 to 4 in the upper field between best and worst members, so we show only the initial field (10/28) and the fifth (12/02) through thirteenth weeks (01/27). For clarity, we highlight key findings:

- The best members develop a strong anticyclone that persists over most of the forecast time-period, contributing to improved prediction of the LCE positioning;
- The best members show active development of cyclones off the Mississippi Fan, assisting in strengthening the DSC cyclone, as well as the eventual separation.

The initial deep fields (10/28) display nearly identical features, with minor deviations from the initial perturbations applied to the upper fields. At Week 6 (12/09) a striking contrast develops between the mean  $\eta_{ref}$  fields for the best and worst members. Here, the best members show prominent, strong anticyclonic and cyclonic features: the anticyclone near the Mississippi Fan, centered at 26.5°N, as well as a developing cyclone beneath the Eastern leg of the LC (centered near 25°N), which is later observed to propagate towards the Deep Southeast Channel (DSC). Both features are present in the worst member mean field; however, the magnitudes are weaker. At Week 8 (12/23), the prominent features in the best members observed in Week 6 remain, whereas the worst members show an anticyclone with significantly decreased intensity, and a cyclone north of it (27.5°N and 87°W). More, the cyclone in the DSC (centered near 24°N and 85°W), although found in both groups, has greater magnitude in the best members.

In Weeks 10 through 12, the best member field retains the signature – and most of the strength – of the Mississippi Fan anticyclone. The DSC cyclone for this group remains, possibly contributing to the initial detachment of Thor on Week 11 (01/13) (Thoppil et al. 2025; Safaei et al. 2025). The worst members retain a weaker DSC cyclone, aiding in predicting a detachment by Week 11 as well. Despite this, the absence of the northern anticyclone results

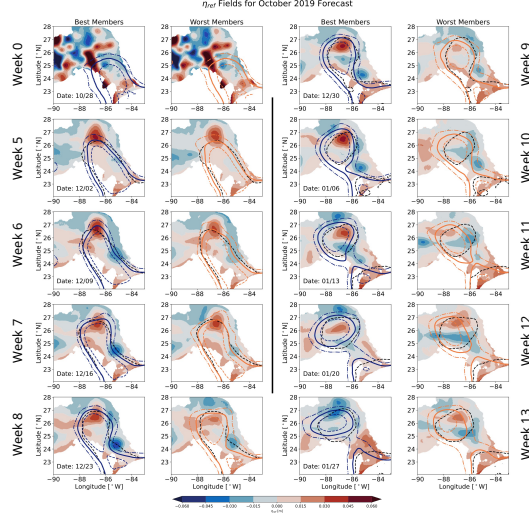


Fig. 7. Mean  $\eta_{ref}$  fields at 2000 m depth for the best (left columns) and worst (right columns) performing members for EF20191028 at Week 0 and Weeks 5–13. Deep cyclones are indicated with blue contours, and anticyclones with red; the upper is represented by three contour levels: the 17-cm contour (thick, solid line) which represents the LC, the -3-cm contour (dot-dashed line), and the 37-cm contour (dashed line) – spanning the central two-thirds of the LC – with the colors differentiating best members (blue) and worst members (orange) as in Fig. 5. For comparison, we include the 17-cm contour (black, dashed line) from the verifying analysis.

in an incorrect prediction of the positioning and orientation of the LCE, demonstrated by the misalignment of the 17-cm contour of the forecast and the verifying analysis (black, dashed line). In contrast, the best member group displays a LCE with better predicted positioning and orientation. Furthermore, in Weeks 11 to 13, we observe a northern cyclone developing off the Mississippi fan (centered at 27.5°N), which is not present in the worst member mean field. These results suggest the worst members are missing deep mesoscale eddies, critical to predicting LCE positioning. Overall, both member groups correctly predict the timing of the initial detachment of LCE Thor, as both maintain a cyclone in the DSC region, but we conjecture the stronger northern anticyclone and DSC cyclone resulted in better prediction of the location of the LCE after detachment for the best members.

## 1) COMPARISON TO DEEP OBSERVATIONS

Figure 8 shows the mean  $\eta_{ref}$  field for the best members (left column), the CPIES (center column), and the worst members (right column). Model fields are limited to the same region as the observations for direct comparison, and we highlight the initial (Week 0) and final (Week 13) weeks of the forecast, as well as two weeks (Weeks 6 and 10) where the best members display better agreement with upper SSH fields (see Fig. 5).

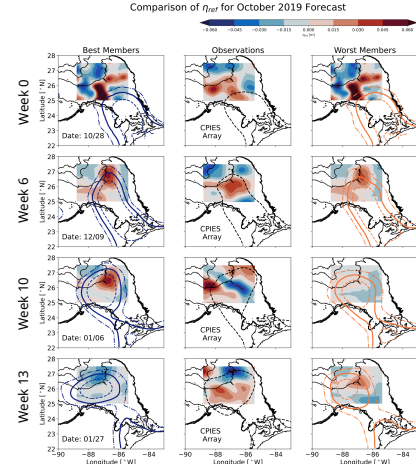


Fig. 8. Weekly intervals of deep mean  $\eta_{ref}$  field for the best performing members (left column), CPIES observation data (center column), and the worst performing members (right column) of EF20191028. The same colors and line-styles as Fig. 7 are used. The models are restricted to the same region as the observations for direct comparison, and bathymetry is provided at 2000, 2500, and 3000 meters depth (solid, black contour lines).

Qualitatively, the initial field for the model agrees well with the observations. The model and observations both display a northern cyclone on the Mississippi Fan (near 27°N) with an anticyclone to the south. At Week 6 (12/09), we find the northern anticyclone seen in the model is present in the observations with similar magnitude. By Week 10 (01/06), the shape of the LC, based on the 17-cm contour is in better agreement for the best members. The observations indicate the anticyclone is propagating west, with another anticyclone moving off the Fan near the upper right edge of the observation area. By the final week of the forecast, the best members continue to show good agreement with the 17-cm contour from the satellite product, in terms of LCE position and orientation; moreover, the observations demonstrate a cyclonic eddy moving off the Mississippi Fan, which is also present in the best member mean field, and absent for the worst members. The observations indicate the model deep field, in the region of the CPIES array, initially agreed well, and it was the best members that continued to display similar, critical features resulting in better agreement in the upper field.

## b. EF20200106: Predicting the Mississippi Fan Cyclone

Mean  $\eta_{ref}$  fields for EF20200106 are given in Fig. 9. As before, we briefly summarize key findings that are explained in greater detail below:

- Both groups develop a cyclone off the Mississippi Fan;

- Best members develop a stronger cyclone earlier in the forecast contributing to improved prediction in the separation and positioning of LCE Thor;
- Worst members develop a strong anticyclone in the DSC, resulting in a misaligned LC and the attachment of the -3-cm contour.

Initial fields are nearly identical, as before, with prominent differences appearing by Week 5 (02/10). Now, the best member mean field displays a strong, northern cyclonic feature (centered near 27.5°N and 87°W) that is also present in the worst member mean field, but with lower magnitude and centered more south and east (26.5°N and 86°W). Further, the best member field displays a cyclonic feature between the LCE and the LC that remains until Week 6 (02/17). In contrast, the worst member field shows an anticyclonic region south of 25°N. Between Week 5 (02/10) and Week 9 (03/09), for the best members we observe the northern cyclone moving south off the Mississippi Fan, and growing stronger. Comparatively, the worst member northern cyclone peaks in magnitude as LCE Thor reattaches (03/16), but weakens over the following weeks (03/23 to 04/06). At this point, an additional cyclonic region appears underneath the LCE. By the time of the reattachment (03/16), both groups maintain a cyclone located near 25.5°N and 87.5°W with similar magnitude, as well as a cyclonic region under the LCE. At Week 12 (03/30), the strength of these features is much greater for the best members, and we observe the cyclone constrained by the Campeche Bank and Mississippi Fan remains stationary through the end of the forecast with consistent strength, whereas it propagates west, losing intensity, for the worst members.

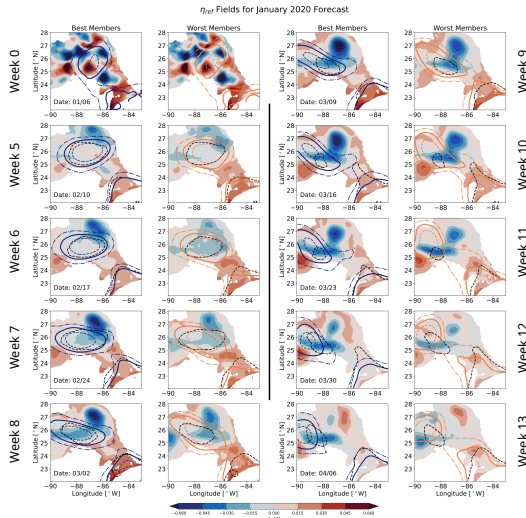


Fig. 9. Weekly intervals of mean  $\eta_{ref}$  field for the best (left columns) and worst (right columns) performing members of EF20200106. Colors and line styles are the same as Fig. 7.

Focusing on the DSC region, at Week 11 we observe a stronger anticyclone at 24°N and 86.5°W for the worst members, which persists until the end of the forecast. For the best members, this feature is absent, only appearing near Week 13. These differences are reflected in the upper field by the positioning of both the path of the LC and the LCE itself. Here, the best members show separation at all SSH contours (-3-cm, 17-cm, and 37-cm), as well as a LC in a port-to-port configuration; this better resembles the 17-cm contour of the verifying analysis. In contrast, the -3-cm contour for the worst members remains attached to the LC, and the LC extends as far north and west as 24.5°N and 87°W, most likely due to the presence of the deep anticyclone.

## 1) COMPARISON TO DEEP OBSERVATIONS

We compare the best and worst member mean fields of  $\eta_{ref}$  to the CPIES array (Fig. 10). The initial (Week 0) fields from the model are found to be in poor agreement compared to the observations, in contrast to the prior forecast. The CPIES array shows a westward anticyclone coupled with an eastern cyclone in the observation region, whereas the model displays cyclonic features in the east and west of the same region, flanked by anticyclonic features to the north and south. At Week 6 (02/17), model magnitudes are significantly lower than the observations. However, both model groups contain a cyclonic feature near the Mississippi Fan (near 27°N), resembling the strong cyclonic feature observed by the CPIES array. Best members show better agreement in orientation and positioning of the LC and LCE. Near the reattachment at Week 10 (03/16), the observations indicate the deep cyclone has propagated south, and is constrained by the bathymetry between the Mississippi Fan and the Campeche Bank (near 25.5°N). For the model, two cyclonic features are present: i) a strong cyclone off the Mississippi Fan; and ii) a cyclone between the Mississippi Fan and the Campeche Bank (near 25.5°N). For the more northern cyclone, the best members display a feature of stronger magnitude, resulting in a deeper trough in the -3-cm contour in contrast to the worst members; however, both fields have weak agreement with the satellite product. By Week 13, the southern, constrained cyclonic feature persists for the best members in a similar position as that observed by the CPIES (found near 25.5°N and 87.5°W), which is missing for the worst members. This aids in the best members showing somewhat better agreement with the 17-cm contour from the satellite product.

Although the initial field was qualitatively different from the observations, both the best and worst member model fields developed the cyclone seen in the observations near the Mississippi Fan on 02/17. This is most likely due to interactions of the LCE and the topography, leading to baroclinic instabilities (Donohue et al. 2016). The timing of the cyclone's development in the model was delayed,

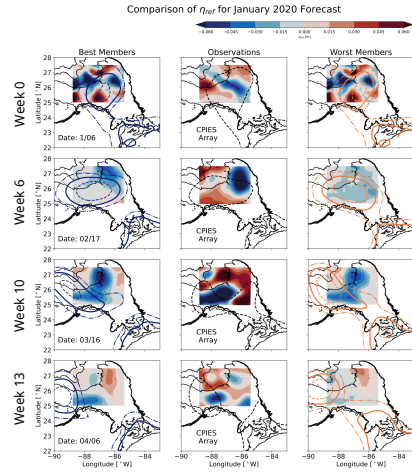


FIG. 10. Weekly intervals of deep mean  $\eta_{ref}$  field for the best performing members (left columns), CPIES observation data (center columns), and the worst performing members (right columns) of EF20200106. We use the same colors, line-styles, and bathymetry as Fig. 9. The models are restricted to the same region as the observations for direct comparison.

leading to an initially weaker, comparatively more northern cyclone, with the worst members showing a more pronounced delay in the development of the cyclonic feature. The model, in both groups, recovers, with the additional cyclonic region forming beneath the LCE. The presence of the strong Mississippi fan cyclone, along with the additional cyclonic region, aids in the reattachment and final separation of LCE Thor in the model. The time-delay and reduced model strength of the northern cyclone most likely led to the contrast between the model SSH field and the verifying analysis (and observations). Further, the poor initialization of the deep field played a role in the delay of the Fan cyclone development, experienced by both the best and worst members; proper initialization of the deep could have prevented such delay. More, this likely resulted in the increased range of uncertainty in SSH, seen in Fig. 6.

## 6. Summary and Implications for Future Forecasts

Deep ( $> 1500$  m depth) mesoscale eddies play an important role in the performance of ensemble forecast members in predicting sea surface height (SSH) in the Loop Current (LC) system in the Gulf of Mexico. Here, 92-day, 32-member ensemble forecasts that span the Loop Current Eddy (LCE) Thor separation event, from October 28th, 2019 through April 6th, 2020 are used. We first identified that smaller uncertainty in the initial deep fields led to an improved SSH forecast. Two forecasts provided case studies, one capturing the initial detachment, the other capturing the reattachment and final separation. With these two forecasts, a simple, yet effective method to rank the performance of individual ensemble forecast members

was developed using root-mean-square-error (RMSE) of SSH against the verifying analysis, as well as SSH from CMEMS satellite product (Fig. 4). With the calculated RMSE values, the best 80<sup>th</sup> and worst 20<sup>th</sup> percentiles of ensemble members over the 13 week forecast time-period were found. The two groups were found to become distinct near Week 5 of the forecast, with the best members typically maintaining lower uncertainty over the forecast time-period (Figs. 5 and 6). Further, the verifying analysis and CMEMS satellite product are both capable of identifying the best and worst members, with both benchmarks indicating the same majority of members.

The deep field was represented by  $\eta_{ref}$ , the 2000 m streamfunction. In both forecasts the deep circulation displayed distinct differences between best and worst members, particularly in the magnitudes and positioning of deep cyclones and anticyclones. Through comparison with deep observations collected with a CPIES array, best members were shown to have better agreement with observed prominent deep features (Figs. 8 and 10). Moreover, when the initial deep field did not agree with observations, the spread of model ocean state realizations increased.

Future forecasts in the Gulf, and more broadly in other boundary current systems, should include deep ocean observations in their assimilation schemes to improve initial ocean states. From the two ensemble forecasts reviewed in the present study, a more realistic deep ocean eddy field has a positive influence on the forecast. In the first case study, the best members displayed better agreement with deep observations (see Figs. 3 and 8). We postulate this initialization in the deep led all ensemble members to better forecast the initial detachment of LCE Thor. However, differences in the evolution of the mean field between the two led to better prediction of SSH in the best member group. In our second case study, the initial deep mean  $\eta_{ref}$  field disagreed with observations (see Figs. 3 and 10). This difference likely led to greater uncertainty in the ensemble, particularly for the worst member group (Fig. 6).

This study reviewed the Thor LCE separation, thus it would be prudent to review other separations with forecasts that have successfully, or unsuccessfully, predicted LCE separation cycles. In addition, these results indicate that deep circulation matters, but our understanding of when and where these observations are most critical for forecast success is not well known. Another study could follow Dukhovskoy et al. (2023) and conduct an Observing System Experiment (OSE) and an Observing System Simulation Experiment (OSSE). For a future OSSE study, it would be beneficial to include an investigation of the role of cyclones in the Deep Southeast Channel (DSC) region, which has been shown to influence LCE separation events (Thoppil et al. 2025; Safaie et al. 2025).

**Acknowledgments.** J.P.C., K.A.D., and D.R.W. acknowledge funding from the US National Academy of Science, Engineering, and Medicine (NASEM) under their Gulf Research Program, UGOS grants, 2000009943 and 200013145. J.P.C., K.A.D., and D.R.W. also acknowledge funding from the US Naval Research Laboratory – Stennis Space Center *via* Office of Naval Research Cooperative Agreement N00173-22-2C005.

**Data availability statement.** The CPIES datasets analyzed for this study can be found in the GRIIDC data repository: <https://data.griidc.org/data/U1.x852.000:0004> and DOI:10.7266/BZ9B3C54.

## APPENDIX A

### Surface Velocity as an Additional Metric

Surface velocity is another parameter which is useful to identify the LC and LCEs, as the 1.5-kt contour is typically taken to represent its frontal edge (Ivanov et al. 2024). Here, we test the use of the surface velocity as an additional measure of model performance, by comparing against velocities taken from the verifying analysis. In both the model and the analysis, we determine the magnitude of the velocity using the longitudinal and meridional components at each surface point, converting from units of meters-per-second to knots before conducting the calculation.

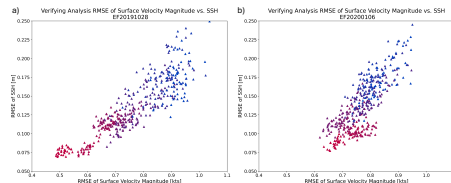


FIG. A1. Scatter plot of weekly RMSE of surface velocity magnitude versus RMSE of SSH for all forecast members of a) EF20191028 and b) EF20200106. Colors correspond to the week from forecast start time, beginning from Week 1 in pink to Week 13 in blue.

We directly investigate the relationship between RMSE of SSH and RMSE of velocity; we plot this for each individual member of the two forecasts, to identify the link between the two parameters and individual member performance. For both forecasts, we observe a linear relationship between RMSE of SSH and RMSE of velocity, indicating that ensemble members that perform well in one metric generally do well in the other. Further, the forecast uncertainty increases with time, as lower, more concentrated RMSE values are found for Week 1 (pink triangles), whereas Week 13 (blue triangles) shows both high RMSE and large spread of possible values. Both surface metrics perform favorably, so we choose to use SSH in our selection process of best and worst members.

## APPENDIX B

### Weighted RMSE Selection

We examined a weighted RMSE metric which used SSH, as well as  $T$ ,  $S$ ,  $U$ , and  $V$  from the upper 500 meters of the water column. Weekly RMSE values were calculated between each ensemble member of the forecast and the verifying analysis at each depth. A weighted RMSE ( $\hat{X}$ ) was calculated using:

$$\hat{X}(z) = \begin{cases} 0.25\text{RMSE}(SSH) + 0.25\text{RMSE}(T) + 0.25\text{RMSE}(S) + 0.125\text{RMSE}(U) \\ 0.375\text{RMSE}(T) + 0.375\text{RMSE}(S) + 0.125\text{RMSE}(U) + 0.125\text{RMSE}(V) \end{cases} \quad (B1)$$

Using  $\hat{X}$  found at each depth, members were ranked using the method outlined in Fig. 4. Despite including more variables and values in the upper 500 meters, this yielded a majority of the same members selected as the best and worst for both forecasts compared against the members selected using RMSE of SSH – for both the verifying analysis and the satellite product from CMEMS. Due to this more complex method selecting members that are not drastically different, we choose to use the simpler method that only requires use of SSH.

## References

- Androulidakis, Y., V. Kourafalou, M. J. Olascoaga, F. J. Beron-Vera, M. Le Hénaff, H. Kang, and N. Ntaganou, 2021: Impact of caribbean anticyclones on Loop Current variability. *Ocean dynamics*, **71** (9), 935–956.
- Bishop, C. H., and Z. Toth, 1999: Ensemble transformation and adaptive observations. *Journal of the atmospheric sciences*, **56** (11), 1748–1765.
- Candela, J., J. Sheinbaum, J. Ochoa, A. Badan, and R. Leben, 2002: The potential vorticity flux through the yucatan channel and the Loop Current in the Gulf of Mexico. *Geophysical Research Letters*, **29** (22), 16–1.
- Chang, Y.-L., and L.-Y. Oey, 2011: Loop Current cycle: Coupled response of the Loop Current with deep flows. *Journal of Physical Oceanography*, **41** (3), 458–471.
- Cornic, M., and J. R. Rooker, 2018: Influence of oceanographic conditions on the distribution and abundance of blackfin tuna (*thunnus atlanticus*) larvae in the Gulf of Mexico. *Fisheries Research*, **201**, 1–10.
- Cummings, J. A., 2005: Operational multivariate ocean data assimilation. *Quarterly Journal of the Royal Meteorological Society: A journal of the atmospheric sciences, applied meteorology and physical oceanography*, **131** (613), 3583–3604.
- Donohue, K., D. Watts, P. Hamilton, R. Leben, and M. Kennelly, 2016: Loop Current Eddy formation and baroclinic instability. *Dynamics of Atmospheres and Oceans*, **76**, 195–216.
- Dukhovskoy, D. S., E. P. Chassignet, A. Bozec, and S. L. Morey, 2023: Assessment of predictability of the Loop Current in the Gulf of

- Mexico from observing system experiments and observing system simulation experiments. *Frontiers in Marine Science*, **10**, 1153 824.
- Dukhovskoy, D. S., R. R. Leben, E. P. Chassignet, C. A. Hall, S. L. Morey, and R. Nedbor-Gross, 2015: Characterization of the uncertainty of Loop Current metrics using a multidecadal numerical simulation and altimeter observations. *Deep Sea Research Part I: Oceanographic Research Papers*, **100**, 140–158.
- E.U. Copernicus Marine Service Information (CMEMS), 1993: Global ocean gridded 1 4 sea surface heights and derived variables reprocessed 1993 ongoing. Accessed on 09 May 2025, <https://doi.org/10.48670/moi-00148>.
- Fox, D., W. Teague, C. Barron, M. Carnes, and C. Lee, 2002: The modular ocean data assimilation system (modas). *Journal of Atmospheric and Oceanic Technology*, **19** (2), 240–252.
- Gilmartin, J., Q. Yang, and H. Liu, 2020: Seasonal abundance and distribution of chaetognaths in the northern Gulf of Mexico: The effects of the Loop Current and mississippi river plume. *Continental Shelf Research*, **203**, 104 146.
- Hamilton, P., 2009: Topographic Rossby waves in the Gulf of Mexico. *Progress in Oceanography*, **82** (1), 1–31.
- Hamilton, P., A. Bower, H. Furey, R. Leben, and P. Pérez-Brunius, 2019: The Loop Current: Observations of deep eddies and topographic waves. *Journal of Physical Oceanography*, **49** (6), 1463–1483.
- Hamilton, P., A. Lugo-Fernández, and J. Sheinbaum, 2016: A Loop Current experiment: Field and remote measurements. *Dynamics of Atmospheres and Oceans*, **76**, 156–173.
- Hiron, L., B. J. de la Cruz, and L. K. Shay, 2020: Evidence of Loop Current frontal eddy intensification through local linear and nonlinear interactions with the Loop Current. *Journal of Geophysical Research: Oceans*, **125** (4), e2019JC015 533.
- Hodur, R. M., 1997: The naval research laboratory's coupled ocean/atmosphere mesoscale prediction system (coamps). *Monthly weather review*, **125** (7), 1414–1430.
- Hurlbut, H. E., and J. D. Thompson, 1982: The dynamics of the Loop Current and shed eddies in a numerical model of the Gulf of Mexico. *Elsevier Oceanography Series*, Vol. 34, Elsevier, 243–297.
- Ivanov, L., R. Arena, A. Bozec, E. Chassignet, S. Longridge, R. Ramos, A. Srinivasan, and M. Iskandarani, 2024: Process-oriented validation of hycom-ts1s reanalysis runs for the northern Gulf of Mexico. *Offshore Technology Conference*, OTC, D021S017R006.
- Johnson Exley, A., K. A. Donohue, D. R. Watts, K. L. Tracey, and M. A. Kennelly, 2022: Generation of high-frequency topographic Rossby waves in the Gulf of Mexico. *Frontiers in Marine Science*, **9**, 1049 645.
- Krishnamurti, T., C. M. Kishtawal, T. E. LaRow, D. R. Bachiochi, Z. Zhang, C. E. Williford, S. Gadgil, and S. Surendran, 1999: Improved weather and seasonal climate forecasts from multimodel superensemble. *Science*, **285** (5433), 1548–1550.
- Laxenaire, R., E. P. Chassignet, D. S. Dukhovskoy, and S. L. Morey, 2023: Impact of upstream variability on the Loop Current dynamics in numerical simulations of the Gulf of Mexico. *Frontiers in Marine Science*, **10**, 1080 779.
- Le Hénaff, M., V. H. Kourafalou, Y. Morel, and A. Srinivasan, 2012: Simulating the dynamics and intensification of cyclonic Loop Current frontal eddies in the Gulf of Mexico. *Journal of Geophysical Research: Oceans*, **117** (C2).
- Le Hénaff, M., and Coauthors, 2021: The role of the Gulf of Mexico ocean conditions in the intensification of hurricane michael (2018). *Journal of Geophysical Research: Oceans*, **126** (5), e2020JC016 969.
- Leben, R. R., 2005: Altimeter-derived Loop Current metrics. *Geophysical Monograph-American Geophysical Union*, **161**, 181.
- Martin, M. J., and Coauthors, 2015: Status and future of data assimilation in operational oceanography. *Journal of Operational Oceanography*, **8** (sup1), s28–s48.
- Martin, P. J., and Coauthors, 2009: User's manual for the navy coastal ocean model (ncom) version 4.0. Tech. rep., Naval Research Laboratory.
- Mellor, G. L., and T. Yamada, 1982: Development of a turbulence closure model for geophysical fluid problems. *Reviews of Geophysics*, **20** (4), 851–875.
- Morey, S. L., and Coauthors, 2020: Assessment of numerical simulations of deep circulation and variability in the Gulf of Mexico using recent observations. *Journal of Physical Oceanography*, **50** (4), 1045–1064.
- National Academies of Sciences and Medicine, 2018: *Understanding and predicting the Gulf of Mexico Loop Current: critical gaps and recommendations*. National Academies Press.
- Nof, D., 2005: The momentum imbalance paradox revisited. *Journal of physical oceanography*, **35** (10), 1928–1939.
- Oey, L.-Y., 2008: Loop Current and deep eddies. *Journal of physical oceanography*, **38** (7), 1426–1449.
- Pérez-Brunius, P., H. Furey, A. Bower, P. Hamilton, J. Candela, P. García-Carrillo, and R. Leben, 2018: Dominant circulation patterns of the deep Gulf of Mexico. *Journal of Physical Oceanography*, **48** (3), 511–529.
- Pichevin, T., and D. Nof, 1997: The momentum imbalance paradox. *Tellus A*, **49** (2), 298–319.
- Rosburg, K. C., K. A. Donohue, and E. P. Chassignet, 2016: Three-dimensional model-observation comparison in the Loop Current region. *Dynamics of Atmospheres and Oceans*, **76**, 283–305.
- Safaie, A., K. Donohue, C. D. Rowley, P. G. Thoppil, and D. R. Watts, 2025: Deep cyclones in the southeast Gulf of Mexico. *Frontiers in Marine Science*, **12**, 1648 949.
- Schmitz Jr, W. J., 2005: Cyclones and westward propagation in the shedding of anticyclonic rings from the Loop Current. *Geophysical Monograph Series*, **161**, 241–261.
- Sheinbaum, J., G. Athié, J. Candela, J. Ochoa, and A. Romero-Arteaga, 2016: Structure and variability of the yucatan and Loop Currents along the slope and shelf break of the yucatan channel and campeche bank. *Dynamics of Atmospheres and Oceans*, **76**, 217–239.
- Stammer, D., M. Balmaseda, P. Heimbach, A. Köhl, and A. Weaver, 2016: Ocean data assimilation in support of climate applications: status and perspectives. *Annual review of marine science*, **8** (1), 491–518.

- Sturges, W., and R. Leben, 2000: Frequency of ring separations from the Loop Current in the Gulf of Mexico: A revised estimate. *Journal of Physical Oceanography*, **30** (7), 1814–1819.
- Thoppil, P. G., C. D. Rowley, P. J. Hogan, and J. Stear, 2025: Evaluating the performance of an ensemble forecast system in predicting Loop Current Eddy separation in the Gulf of Mexico. *Progress in Oceanography*, 103529.
- Thoppil, P. G., and Coauthors, 2021: Ensemble forecasting greatly expands the prediction horizon for ocean mesoscale variability. *Communications Earth & Environment*, **2** (1), 89.
- Tsei, S., S. Howden, A.-R. Diercks, J. A. Zhang, T. N. Miles, E. Nyadjro, and K. M. Martin, 2025: Low salinity, high ocean heat content, and warm core eddy effects on the upper ocean response during hurricane sally (2020): An analysis of a hurricane glider observations and coupled atmosphere-ocean model. *Journal of Geophysical Research: Oceans*, **130** (10), e2024JC021470.
- Watts, D. R., X. Qian, and K. L. Tracey, 2001: Mapping abyssal current and pressure fields under the meandering gulf stream. *Journal of Atmospheric and Oceanic Technology*, **18** (6), 1052–1067.
- Wei, M., Z. Toth, R. Wobus, and Y. Zhu, 2008: Initial perturbations based on the ensemble transform (et) technique in the ncep global operational forecast system. *Tellus A: Dynamic Meteorology and Oceanography*, **60** (1), 62–79.
- Wei, M., Z. Toth, R. Wobus, Y. Zhu, C. H. Bishop, and X. Wang, 2006: Ensemble transform kalman filter-based ensemble perturbations in an operational global prediction system at ncep. *Tellus A: Dynamic Meteorology and Oceanography*, **58** (1), 28–44.
- Wei, M., and Coauthors, 2016: The performance of the us navy's relo ensemble, ncom, hycom during the period of glad at-sea experiment in the Gulf of Mexico. *Deep Sea Research Part II: Topical Studies in Oceanography*, **129**, 374–393.